

Optimal parameter space for stabilizing the ferroelectric phase of $Hf_{0.5}Zr_{0.5}O_2$ thin films under strain and electric fields

Lvjin Wang(王侣锦), Cong Wang(王聪), Linwei Zhou(周霖蔚), Xieyu Zhou(周谐宇), Yuhao Pan(潘宇浩), Xing Wu(吴幸), and Wei Ji(季威)

Citation: Chin. Phys. B, 2024, 33 (**7**): 076803. DOI: 10.1088/1674-1056/ad498b
Journal homepage: http://cpb.iphy.ac.cn; http://iopscience.iop.org/cpb

What follows is a list of articles you may be interested in

Molecular beam epitaxy growth of quantum devices

Ke He(何珂)
Chin. Phys. B, 2022, 31 (**12**): 126804. DOI: 10.1088/1674-1056/aca6d3

In-plane optical anisotropy of two-dimensional VOCl single crystal with weak interlayer interaction

Ruijie Wang(王瑞洁), Qilong Cui(崔其龙), Wen Zhu(朱文), Yijie Niu(牛艺杰), Zhanfeng Liu(刘站锋), Lei Zhang(张雷), Xiaojun Wu(武晓君), Shuangming Chen(陈双明), and Li Song(宋礼)
Chin. Phys. B, 2022, 31 (**9**): 096802. DOI: 10.1088/1674-1056/ac7555

Surface electron doping induced double gap opening in T_d-WTe_2

Qi-Yuan Li(李启远), Yang-Yang Lv(吕洋洋), Yong-Jie Xu(徐永杰), Li Zhu(朱立), Wei-Min Zhao(赵伟民), Yanbin Chen(陈延彬), and Shao-Chun Li(李绍春)
Chin. Phys. B, 2022, 31 (**6**): 066802. DOI: 10.1088/1674-1056/ac632e

C_9N_4 as excellent dual electrocatalyst: A first principles study

Wei Xu(许伟), WenWu Xu(许文武), and Xiangmei Duan(段香梅)
Chin. Phys. B, 2021, 30 (**9**): 096802. DOI: 10.1088/1674-1056/ac0ccf

Epitaxial growth of antimony nanofilms on HOPG and thermal desorption to control the film thickness

Shuya Xing(邢淑雅), Le Lei(雷乐), Haoyu Dong(董皓宇), Jianfeng Guo(郭剑峰), Feiyue Cao(曹飞跃), Shangzhi Gu(顾尚志), Sabir Hussain, Fei Pang(庞斐), Wei Ji(季威), Rui Xu(许瑞), Zhihai Cheng(程志海)
Chin. Phys. B, 2020, 29 (**9**): 096801. DOI: 10.1088/1674-1056/aba27c

---

Optimal parameter space for stabilizing the ferroelectric phase of $Hf_{0.5}Zr_{0.5}O_2$ thin films under strain and electric fields

Lvjin Wang(王侣锦)[1,2,†], Cong Wang(王聪)[1,2,†], Linwei Zhou(周霖蔚)[1,2], Xieyu Zhou(周谐宇)[1,2], Yuhao Pan(潘宇浩)[1,2], Xing Wu(吴幸)[3,‡], and Wei Ji(季威)[1,2,§]

[1] *Beijing Key Laboratory of Optoelectronic Functional Materials & Micro-Nano Devices, Department of Physics, Renmin University of China, Beijing* 100872, *China*

[2] *Key Laboratory of Quantum State Construction and Manipulation (Ministry of Education), Renmin University of China, Beijing* 100872, *China*

[3] *In Situ Devices Center, School of Integrated Circuits, East China Normal University, Shanghai* 200241, *China*

(Received 25 January 2024; revised manuscript received 18 April 2024; accepted manuscript online 10 May 2024)

Hafnia-based ferroelectric materials, like $Hf_{0.5}Zr_{0.5}O_2$ (HZO), have received tremendous attention owing to their potentials for building ultra-thin ferroelectric devices. The orthorhombic(O)-phase of HZO is ferroelectric but metastable in its bulk form under ambient conditions, which poses a considerable challenge to maintaining the operation performance of HZO-based ferroelectric devices. Here, we theoretically addressed this issue that provides parameter spaces for stabilizing the O-phase of HZO thin-films under various conditions. Three mechanisms were found to be capable of lowering the relative energy of the O-phase, namely, more significant surface-bulk portion of (111) surfaces, compressive *c*-axis strain, and positive electric fields. Considering these mechanisms, we plotted two ternary phase diagrams for HZO thin-films where the strain was applied along the in-plane uniaxial and biaxial, respectively. These diagrams indicate the O-phase could be stabilized by solely shrinking the film-thickness below 12.26 nm, ascribed to its lower surface energies. All these results shed considerable light on designing more robust and higher-performance ferroelectric devices.

Keywords: $Hf_{0.5}Zr_{0.5}O_2$, orthorhombic phase, ferroelectric films, phase stability, thickness-dependent, ternary phase diagrams

PACS: 68.65.–k, 77.80.–e, 85.50.–n **DOI:** 10.1088/1674-1056/ad498b

1. Introduction

Ultra-thin ferroelectric films are usually required to build miniaturized nonvolatile memories[1,2] such as ferroelectric random access memories (FeRAM)[3,4] and ferroelectric field effect transistors (FeFET)[5–8] However, downsizing conventional perovskite-based ferroelectric films is always difficult because of strong depolarization fields in perovskite-based thin-films.[9–11] Zirconium-doped hafnia ($Hf_{0.5}Zr_{0.5}O_2$, HZO) thin-films have attracted substantial research interests recently, ascribed to their advantages of stable ferroelectricity in the nanoscale thickness,[12,13] strong remnant polarization,[14–16] and exceptional complementary metal–oxide–semiconductor (CMOS) compatibility.[17,18] HZO has various polymorphs in the bulk phase depending on temperature and pressure conditions, the most stable phase is the monoclinic phase (M-phase, space group $P2_1/c$),[19,20] transition to the tetragonal phase (T-phase, space group $P4_2/nmc$)[21] occurs at 1973 K, and further transition to the cubic phase (C-phase, space group $Fm\bar{3}m$)[22] occurs at 2773 K.[23] At room temperature, applying hydrostatic pressure exceeding 4.3 GPa results in a transformation to a centrosymmetric orthorhombic phase (space group *Pbca*).[24] However, all of these bulk phases possess inversion symmetry and cannot exhibit ferroelectric behavior, the origin of the ferroelectricity in HZO is attributed to another metastable non-centrosymmetric orthorhombic phase (O-phase, space group $Pca2_1$).[25,26] In general, the M- and O-phases are more commonly observed in experiments.[5,14,27–29] These two phases compete with each other in energy and/or growth kinetics,[30,31] giving rise to coexisted M- and O-phases in HZO thin-films grown using either the atomic layer deposition (ALD),[32–35] or the pulsed laser deposition (PLD),[36] or the magnetron sputtering technique.[37] Relatively small portion of the O-phase is a major issue for the performance far less than the ideal in ferroelectric devices built with HZO thin-films.[9,28,38,39] Therefore, further stabilizing the O-phase to increase its portion in prepared HZO thin-films becomes the primary challenge to improve the performance of HZO ferroelectric devices.[4,8]

Many attempts have been used to stabilize the ferroelectric O-phase in the past decades, including dopants,[27,33,40,41] oxygen vacancies,[42–44] mechanical stress,[45–50] electric field,[51–54] crystallographic orientation,[46,55] and annealing or depositing temperature.[56–59] All these routes essentially tune the relative free energy of the two phases.[20,30,43] In ferroelectric devices, HZO is prepared in thin-films of specific thicknesses, with the increase of HZO thickness, phase

[†]These authors contributed equally to this work.

[‡]Corresponding author. E-mail: xwu@cee.ecnu.edu.cn

[§]Corresponding author. E-mail: wji@ruc.edu.cn

© 2024 Chinese Physical Society and IOP Publishing Ltd

transition from the O-phase to the M-phase occurs. This thickness-dependent behavior has been observed in many experiments,[15,47,60] but a comprehensive theoretical explanation for this behavior is yet to be unveiled. An interesting question additionally arises whether the thin-film thickness, together with these external fields, could efficiently affect the relative stabilities of those phases in HZO films.

Here, we investigated the relative stability and critical conditions of different phases of HZO films by considering film-thickness, strain, and electric field using DFT calculations. We first plotted binary phase diagrams as functions of lattice constant and electric field to illustrate the phase stability between the M- and O-phases. Our findings indicated that the ferroelectric O-phase is preferred under *c*-axis compressive strains and positive electric fields. Next, we systematically calculated the surface energy for various low-index surfaces of the O- and M-phases to explore the thickness-dependent phase stability. The results indicate that a thinner (111) slab could further stabilize the O-phase. Given these results, we depicted ternary phase diagrams by incorporating the film-thickness as the third dimension into our binary phase diagrams, providing a more intuitive representation of the critical conditions for the O-phase.

2. Methods

2.1. Density functional theory calculations

Density functional theory (DFT) calculations were performed using the generalized gradient approximation (GGA) for the exchange–correlation potential, the projector augmented-wave (PAW) method[61,62] and a plane-wave basis set as implemented in the Vienna *ab-initio* simulation package (VASP).[63,64] Dispersion correction was made at the van der Waals density functional (vdW-DF) level,[65,66] using the optB86b functional for the exchange potential, which was proven to be accurate in describing the structural properties of the layered materials[67–71] and was adopted for structure-related and electric polarization calculations. The kinetic energy cut-off for the plane-wave basis sets was set to 700 eV for the geometry relaxations and 600 eV for electric polarization and energy calculations. The shapes and volumes of each cell were fully relaxed until the residual force per atom was less than 0.005 eV/Å. An $8\times8\times8$ *k*-mesh was used for sampling the Brillouin zone (BZ) for the $Hf_{0.5}Zr_{0.5}O_2$ bulk phases. The relative permittivity is calculated using density functional perturbation theory (DFPT)[72–74] while the electric polarization P is calculated using the Berry phase method as implemented in VASP,[75–77] which is defined as $P = P_{\text{ion}} + P_{\text{elec}}$, where P_{ion} and P_{elec} refer to the ionic and electronic contributions, respectively. In surface energy calculations, a vacuum layer was used to reduce interactions among adjacent image layers and we found that a vacuum layer of 20 Å was sufficient to ensure the surface energy convergence within 0.001 eV/Å^2.[78] A dipole correction along the z direction is considered to correct the artificial electric polarization introduced by the periodic boundary condition and to balance the vacuum level differences on the different sides of the $Hf_{0.5}Zr_{0.5}O_2$ slabs.[79,80] A series of strains were applied in the range of -8.0% to 8.0% in a step of 1.0%. An electric field was applied along the c axis in the range of -0.80 V/nm to $+0.80$ V/nm in a step of 0.05 V/nm.

2.2. Surface energy

The surface energy (E_{surf}) was calculated as[81,82]

$$E_{\text{surf}} = \frac{(E_{\text{slab}} - N_{\text{Hf}}E_{\text{bulk}}^{\text{HfZrO}_4} - (N_{\text{Oxygen}} - 4N_{\text{Hf}})\mu_{\text{Oxygen}})}{2A}, \quad (1)$$

where E_{slab} represents the total energy of the HZO slab, $E_{\text{bulk}}^{\text{HfZrO}_4}$ is the energy for bulk $HfZrO_4$ per formula unit, and A is the surface area. N_{Oxygen} and N_{Hf} are numbers of oxygen and Hf atoms in the HZO slab, thus $N_{\text{Oxygen}} - 4N_{\text{Hf}}$ equals excessive oxygen beyond stoichiometric $HfZrO_4$ units in the slab. μ_{Oxygen} is the chemical potential of the oxygen, which is in a range estimated using $\mu_{\text{Oxygen}} = \mu_{\text{O}} + \Delta\mu_{\text{Oxygen}}$ where μ_{O} is the half of the total energy of one O_2 gas-phase molecule, and $\Delta\mu_{\text{Oxygen}}$ is thus the formation energy per O of $HfZrO_4$. Therefore, the surface energy of either phase has two extremes: $\Delta\mu_{\text{Oxygen}} = 0$ and $\Delta\mu_{\text{Oxygen}} = 1/4\Delta\mu_{\text{tot}}$, which correspond to the oxygen-rich and oxygen-deficient conditions, respectively, where $\Delta\mu_{\text{tot}}$ represents the formation energy of bulk $HfZrO_4$.

The new in-plane lattice vectors $\boldsymbol{u}$ and $\boldsymbol{v}$ of the (111) surface are along the $[1\bar{1}0]$ and $[10\bar{1}]$ directions, respectively. The projected angle θ between the original lattice vector $\boldsymbol{a}$ and the new lattice vector $\boldsymbol{u}$ is calculated by $\cos\theta = (\boldsymbol{a}\cdot\boldsymbol{u})/(|\boldsymbol{a}|\cdot|\boldsymbol{u}|)$.

2.3. Temperature-dependent free energy

The temperature-dependent free energy, F, of each phase was derived using the formula following a previously developed approach:[83,84]

$$F = U + \sum_i \left\{ \frac{1}{2}\hbar\omega_i + k_{\text{B}}T\ln\left[1 - \exp\left(-\frac{\hbar\omega_i}{k_{\text{B}}T}\right)\right]\right\}, \quad (2)$$

where the first term U represents the total energy calculated using DFT. The zero-point energy and the vibrational entropy are the second and third terms, respectively, which are derived using the quasi-harmonic vibrational frequencies calculated using density functional perturbation theory (DFPT). Here ω_i, k_{B}, and T are the vibrational frequency, Boltzmann constant, and temperature, respectively.

3. Results and discussion

3.1. Crystal structure and uniaxial-, biaxial-strain effects

We modeled the HZO bulk structures by replacing two Hf atoms with two Zr atoms in the unit cell of the M (Figs. 1(a)–

1(c)) or O (Figs. 1(d)–1(f)) phase of bulk HfO_2. We considered different inequivalent substituting sites for the two Zr atoms, among which the shown two are the energetically most stable. Details of the energy comparison are available in supporting information of Fig. S1 and Table S1. The M-phase exhibits higher structural symmetry, larger volume, and better stability (0.17 eV/u.c.) than the O-phase. Details of the comparisons are documented in Table 1. Their fully relaxed lattice constants are $a = 5.12$ Å, $b = 5.21$ Å, and $c = 5.29$ Å for the M-phase, and $a = 5.05$ Å, $b = 5.27$ Å, and $c = 5.07$ Å for the O-phase. All these values are comparable to previously reported theoretical[20,85] and experimental[14,19,20,85,86] values. Although the values for constant a (or b) differ within 1% between the two phases, lattice constant c of the M-phase is 4.3% larger than that the O-phase, namely 5.29 Å (M) versus 5.07 Å (O). We thus infer that a compressive strain applied along the c axis could, most likely, lead to a phase transition from the M-phase to the O-phase. In other words, it is expected that the metastable O-phase (ferroelectric phase) could be stabilized by a compressive strain applied along the c axis, which deserves further clarification.

Table 1. Calculated parameters for HZO phases. a, b, and c are the lattice constants as denoted in Fig. 1, α, β, and γ are the angle between lattice vectors b and c, a and c, a and b, respectively. V, ΔU, ε_r, P, and E_g represent the cell volume, total energy difference per unit cell, relative permittivity, spontaneous polarization, and bandgaps, respectively.

Phase	a (Å)	b (Å)	c (Å)	α (°)	β (°)	γ (°)	V (Å^3)	ΔU (eV)	ε_r	P (μC/cm^2)	E_g (eV)
M	5.12	5.21	5.29	90.00	99.30	90.00	139.60	0.00	17.91	0.00	5.18
O	5.05	5.27	5.07	90.00	90.00	90.00	135.02	0.17	21.01	54.00	5.15

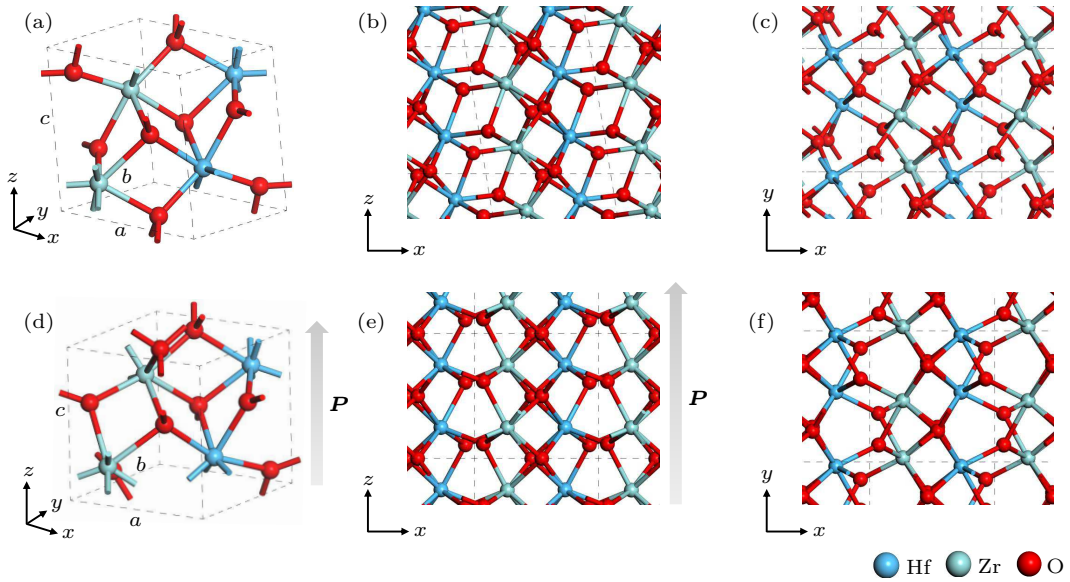


Fig. 1. Schematic models of bulk HZO. (a)–(c) Perspective, side, and top views of the M-phase. (d)–(f) Perspective, side, and top views of the O-phase. Blue, light green, and red balls represent Hf, Zr, and O atoms, respectively. The direction of the spontaneous polarization (polar-axis) of the O-phase is denoted by the grey arrow, which is almost along the c axis.

Figure 2(a) plots the free energies of the M- and O-phases as a function of the lattice constant c. Under compressive uniaxial strain along the c axis, the M-phase, as we expected, undergoes a first-order transition to the O-phase at approximately -3.0% c-strain. A collapse occurs for the c axis of the M-phase that lattice constant c decreases from 5.13 Å (-3.0%) of the M-phase to 4.97 Å (-2.0%) of the O-phase. Such compressive strain could be achieved in experiments through densification upon crystallizing,[60,87] or lattice mismatch,[88,89] or difference in the thermal expansion coefficients[90,91] between the HZO thin-films and its substrates or electrodes. It is important to note that the c axis here does not necessarily align with the out-of-plane (OOP) direction of the films, its orientation depends on the specific growth conditions in the experiments.[29] The a-axis or b-axis uniaxial strain, however, does not show a phase transition in a reasonable strain range as plotted in Fig. S2 of supporting information. For the biaxial strain, crossover of free energies was also found for the ac (see Fig. S2(b)) or bc plane (see Fig. S2(d)), but was not in the ab-plane case (see Fig. S2(c)).

3.2. The influence of external electric field

The O-phase is electrically polarized, and electric fields are applied in operating devices containing HZO films. It is thus straightforward to consider the role of external electric fields in determining the relative stability of the O-phase in

HZO films. An experiment[28] shows that the O-phase gradually transformed to the M-phase under an electric field of at least 0.3 V/nm applied along the negative c axis (the $[00\bar{1}]$ direction) in HZO films grown along the [001] direction on a monocrystalline silicon substrate. This transition leads to a decreased (increased) percentage of the ferroelectric O-phase (non-polar M-phase), resulting in a degradation of the ferroelectric performances of HZO thin-films.

To further clarify the role of electric fields, we have noted that in a system with charged defects, electric fields can induce the redistribution of these defects, thereby influencing the phase stability.[92,93] However, in the case of this study without defects, the primary effect of the electric field is to alter the potential energy of electric dipole moment.[94,95] Therefore, we only included an electric field term[30,96] in our free energy. It reads as

$$F = U - V(\varepsilon_r \varepsilon_0 \boldsymbol{E} + \boldsymbol{P}) \cdot \boldsymbol{E}, \tag{3}$$

where U is the total energy calculated by DFT, V is the bulk volume, $\boldsymbol{E}$ is the electric field, $\boldsymbol{P}$ is the spontaneous polarization, ε_r (ε_0) is the relative (vacuum) permittivity (see Table 1 for more details).

Figure 2(c) plots the free energies of the M- (blue) and O-phases (red) in their strain-free geometries as a function of the electric field applied parallel (positive values) or anti-parallel (negative values) to the c axis. The free energy of the M-phase decreases under electric fields in either direction, ascribed to its non-polar character. The spontaneous electric polarization of the O-phase was set to be parallel to the c direction in the free energy plot (Fig. 2(c)). Its free energy initially increases and subsequently decreases under the electric field anti-parallel to the c direction (negative fields), clearly identifying its non-zero spontaneous polarization ($\boldsymbol{P} \approx 54\ \mu C/cm^2 \cdot \boldsymbol{c}$, where $\boldsymbol{P}_{ion} \approx 16\ \mu C/cm^2 \cdot \boldsymbol{c}$ and $\boldsymbol{P}_{elec} \approx 38\ \mu C/cm^2 \cdot \boldsymbol{c}$). This value is comparable to the spontaneous polarization reported for the HfO_2 O-phase, namely $\boldsymbol{P} = 52\ \mu C/cm^2 \cdot \boldsymbol{c}$.[85] Notably, the O-phase becomes more stable than the M-phase under a positive electric field beyond 0.39 V/nm. These results indicate that under the action of a negative electric field, the polarization direction of the O-phase has not been reversed before it has been transformed into the M-phase, thus losing its ferroelectricity. Therefore, the O-phase of bulk HZO is fragile under negative external electric fields, which appears to be one of the major issues leading to the failure of HZO layers in ferroelectric devices. Thus, it poses a challenge to the community, to find a strategy for remedying this failure.

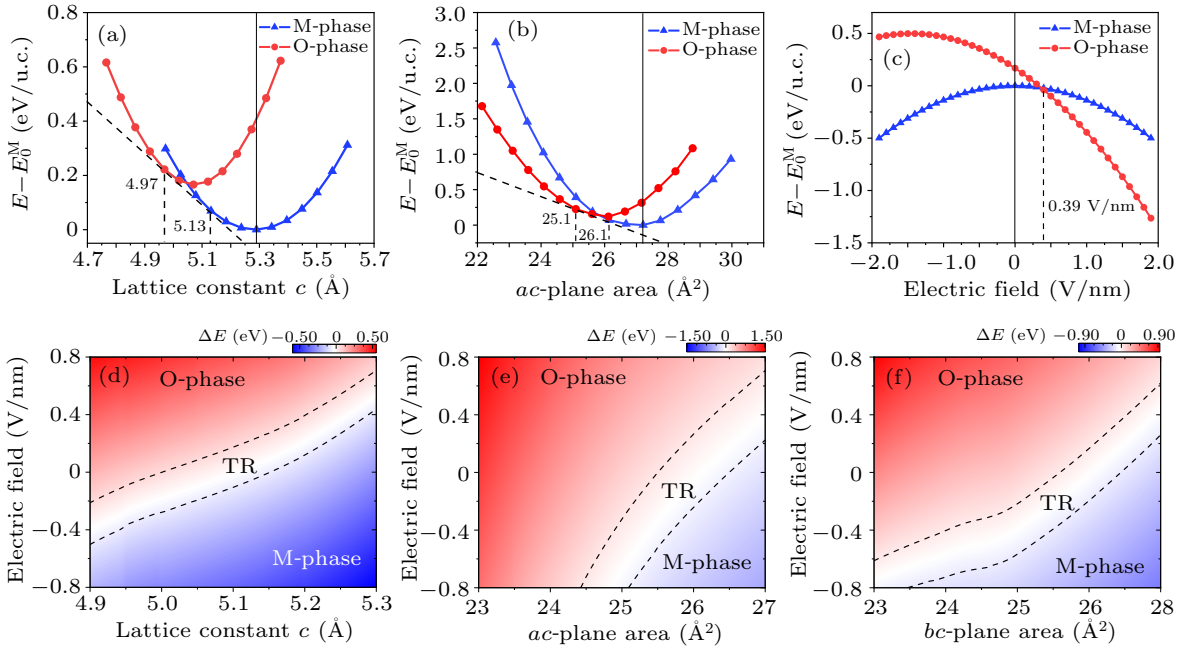


Fig. 2. Free energy curves and binary phase diagrams of the HZO phases. (a)–(b) Free energy differences vary with the lattice constant c and the ac-plane area, respectively. The black dashed lines represent the common tangent lines. (c) Free energy differences vary with applying an external electric field along the c axis in strain-free states. For M-phase and O-phase, the free energy of the equilibrium bulk is shown as blue triangle and red circle lines, respectively. The energy of the M-phase in ground state was set to be the reference. (d)–(f) Binary phase diagrams for the c-axis electric field and the lattice constant c (d), ac-plane area (e), and bc-plane area (f), respectively. The colors show the difference in free energy between the M- and O-phases, the blue (negative) region denotes the favored M-phase (non-polar phase), the red (positive) region denotes the favored O-phase (ferroelectric phase), the white region denotes the phase transition region, the black dashed lines represent the boundaries of the phase transition.

We infer that a combination of strain and electric field could be a strategy to address this issue, as they play substantial roles in tuning the relative stability of the M and O-phases (see Figs. 2(a)–2(c)). We plotted binary phase diagrams for their stability as functions of electric field and lattice constant c (Fig. 2(d)), ac-plane (Fig. 2(e)), and bc-plane (Fig. 2(f)) areas.

These phase diagrams show similar trends regardless of the way of applying strains. In particular, the O-phase favors high compressive strains and large positive electric fields, whereas the M-phase prefers low compressive or tensile strain and negative electric fields. Therefore, an enlarged compressive strain or/and a reduced negative electric field are more prone to suppress the O-to-M phase transition. A striking result lies in that a sufficiently large compressive strain, e.g., 24.8 Å^2 *ac*-plane area for the O-phase, whose initial area is 25.6 Å^2 (Fig. 2(e)), could effectively uphold the stability of the O-phase regardless being placed under positive or negative electric fields up to ±0.40 V/nm. It has been reported that the coercive field and breakdown electric field in HZO devices are approximately 0.1 V/nm[97] and 0.4 V/nm,[98] respectively, at room temperature. Therefore, this strain-promoted robustness of ferroelectricity guarantees the feasibility of reversing its spontaneous polarization direction under applied reasonably large electric fields.[99,100]

3.3. Thickness dependence

Previous experiments suggested that the relative stability of the O- and M-phases has thickness dependence that the thinner of the HZO film, the more portion of the O-phase,[101,102] implying competition among the surface and bulk energies of the two phases. We thus plotted surface energy differences for various low-index surfaces with likely surface terminations of these two phases in Fig. 3(a) (see Fig. S3 for details in supporting information). For those surfaces not satisfying the stoichiometric condition, we considered their surface energies under the oxygen-rich and oxygen-deficient extremes (see Section 2 for details).

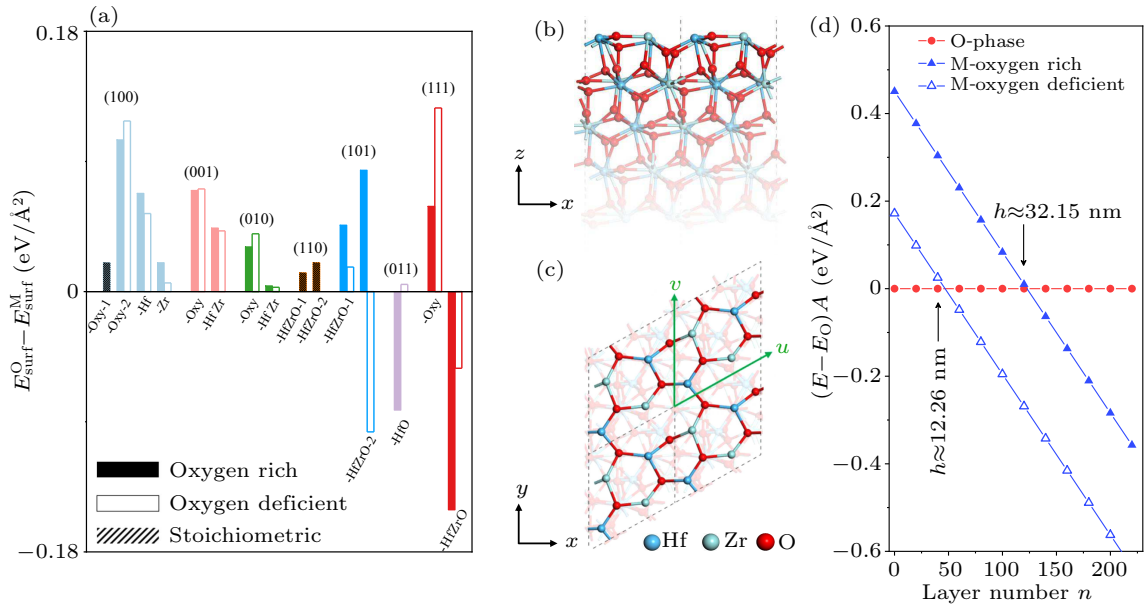


Fig. 3. Surface energies and thickness-dependent phase stability. (a) Surface energy differences histograms of the various low-index surfaces with likely surface terminations in HZO slabs. The surface energies of (100), (001), (010), (110), (101), (011), and (111) surfaces are represented by light blue, pink, green, orange, blue, purple, and red respectively. The labels "-Oxy", "-Hf", "-Zr", "-HfZr", and "-HfZrO" refer to oxygen, hafnium, zirconium, hafnium–zirconium, and hafnium–zirconium–oxygen terminations, respectively. Solid, hollow, and striated histograms represent the oxygen-rich, oxygen-deficient, and stoichiometric cases, respectively. The surface energies of the M-phase were set to be the reference. (b)–(c) Side and top views of the O-phase (111) surface terminate in Hf, Zr, and O atoms ((111)-HfZrO), with only surface atoms being opaque, the green arrows represent the new in-plane lattice vectors of the surface. (d) Evolution of the phase stability with layer thickness without strain or electric field. Energy differences per surface area for M-phase under the oxygen-rich and oxygen-deficient conditions are plotted with solid and hollow blue triangles, respectively. The unit area energy of the O-phase is plotted for reference. The black arrows are corresponding to the critical thickness of the O-phase.

Among all considered surfaces, three of them, namely (101)-HfZrO-2 (blue, right), (011)-HfO (purple), and (111)-HfZrO (red, right) (see Table S2 for details in supporting information) are energetically more preferred in the O-phase than in the M-phase, as plotted in Fig. 3(a). Among them, only the Hf–Zr–O terminated (111) surface [(111)-HfZrO] of the O-phase is preferred under both oxygen-rich and oxygen-deficient conditions, the side- and top-views of which were depicted in Figs. 3(b) and 3(c), respectively. This result suggests that the O-phase could be further stabilized in a thinner (111) slab, but the critical thicknesses, especially those under strain and electric field, are yet to be determined. Therefore, we focus solely on the (111) slabs in comparing the bulk and surface energies of the two HZO phases.

To determine the critical thickness for stabilizing the O-phase, we considered the total energy difference (ΔE) between the two phases in specific thicknesses, which reads as follws:[103,104]

$$\Delta E = n\left(E^{M}_{bulk} - E^{O}_{bulk}\right) + 2A\left(E^{M}_{surf} - E^{O}_{surf}\right), \tag{4}$$

in which n represents the number of layers (thickness), A

is the surface area, E_{bulk} (E_{surf}) is bulk (surface) energy per formula unit. Figure 3(d) plots ΔE per surface area as a function of the number of layers n for the oxygen-rich and oxygen-deficient conditions. The critical thicknesses h were predicted to be approximately 12.26 nm and 32.15 nm for the oxygen-deficient and oxygen-rich extremes, respectively, which fully cover most previously reported experimental values, e.g., 14.5,[105] 20,[47] and 30 nm.[15] It should be noted that the thickness-induced phase transition we explored here based on the (111) surface is qualitatively consistent with the generally accepted experimental conclusion that ferroelectric properties are altered by changing grain size.[106,107] As we mentioned earlier that either polar-axis electric field or c strain can tune the relative stability of the O- and M-phases. They thus affect the critical thickness of the layer thickness determined M–O phase transition. We incorporated a third dimension (thickness) into the previously established binary phase diagrams, plotting them in ternary phase diagrams in Fig. 4. It should be noted that the normal vector $\boldsymbol{n}$ (OOP direction) of the HZO films at this time is [111], the real situation in experiments are that substrates or electrodes can provide in-plane (IP) strain for HZO, while the electric field is applied along the OOP direction. Therefore, the predicted strain and electric field values in the above binary phase diagrams need to be projected onto the new IP lattice vectors ($|\boldsymbol{u}| = 7.29$ Å and $|\boldsymbol{v}| = 7.16$ Å) and the OOP lattice vector ($\boldsymbol{n}$), respectively (see Section 2 for details).

Figure 4 depicts the free energy difference per surface area between the M- and O-phases ($\Delta F = (E_{\text{M-phase}} - E_{\text{O-phase}})/A$) as functions of the lattice constant v (uv-plane area were available in Fig. S4 in supporting information), the electric field applied parallel to the OOP direction, and the (111) slab thickness. Figures 4(a) and 4(4b) plot the ternary phase diagram of uniaxial v-axis strain case in the oxygen-rich (oxygen-deficient) limit. The O-phase is more stable in the upper left corner of the diagram, which favors compressive strain, positive electric field, and thin thickness. For example, the data point ($v = 6.67$ Å, $E_{\text{field}} = 0.00$ V/nm, $h = 8.25$ nm) marked by the yellow dot in Fig. 4(a) indicates the area-normalized free energy of the O-phase is 0.46 eV/Å^2 lower than that of the M-phase. In this specific thickness and strain, the O-phase persists even under either positive or negative OOP electric fields up to 0.40 V/nm, allowing to efficiently switch the polarization direction and thereby ensuring the ferroelectric functions. Oxygen deficiency weakens the robustness of the pristine O-phase in the HZO slabs during the growth process. If not considering the formation of likely oxygen vacancies nor breakdown effects, the O-phase thin-film (the yellow dot in Fig. 4(b), with 6.67-Å lattice constant v & 8.25-nm thickness) would gradually transform into the M-phase when the applied electric field approached −0.59 V/nm. Upon formation of oxygen vacancies,[43] it is noteworthy that although the total energy of the O-phase remains higher than that of the M-phase as the concentration of oxygen vacancies increases (up to 12.5%), the total energy difference between the O-phase and M-phase notably diminishes (see Fig. S5(c) in supporting information). At the same time, the formation energy of the O-phase consistently remains lower than that of the M-phase (see Fig. S5(d) in supporting information). Therefore, if HZO generates oxygen vacancies under the oxygen-deficient condition, the formation of the O-phase becomes more feasible under the same conditions.

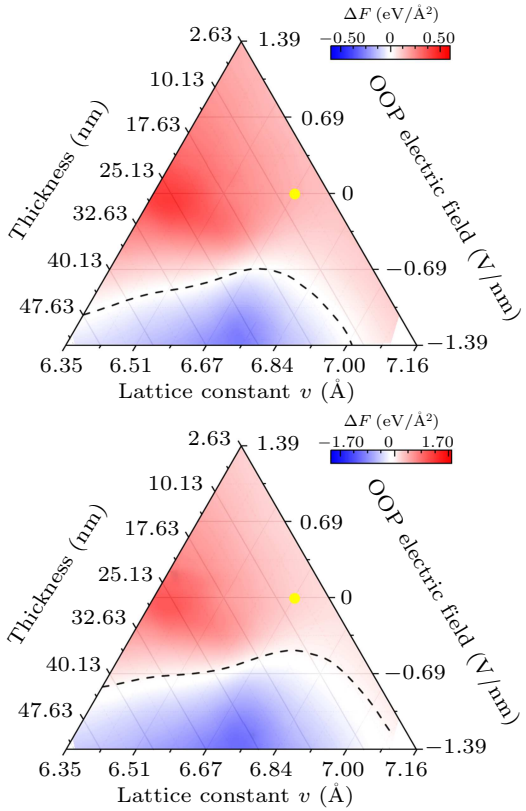


Fig. 4. Ternary phase diagrams of the HZO phases as functions of lattice constant v, electric field, and thickness. The free energy difference per surface area was calculated for the (111)-HfZrO surface in the oxygen-rich condition (a) and in the oxygen-deficient condition (b). The colors indicate the free energy difference per surface area between the M- and O-phases ($\Delta F = (E_{\text{M-phase}} - E_{\text{O-phase}})/A$), with the blue (negative) region denotes the favored M-phase and the red (positive) region denotes the favored O-phase. The black dashed line represents the boundary between the M- and O-phases.

In the atomic limit where the thickness of the (111) HZO slab was minimized to one-unit cell (~ 0.26 nm), which is comprised of two surfaces solely. The O-phase predominates the one-unit-cell slab and exhibits remarkable stability. Particularly, the strain-free one unit-cell-thick (111) slab of the O-phase is 0.16 eV/Å^2 (oxygen-deficient) to 0.44 eV/Å^2 (oxygen-rich) more stable than that of the M-phase, which are sufficient to prevent the O-to-M transition even in the presence of an OOP negative electric field up to 0.40 V/nm solely. Thus, the ternary phase diagrams in Fig. 4 could provide a suitable selection interval for growing or optimiz-

ing the high-performance HZO ferroelectric devices. It is worth noting that HZO films commonly exhibit polycrystalline structures, and the successful fabrication of single crystal structures through ALD or PLD techniques in experiments is rare.[108,109] However, employing epitaxial growth techniques allows for the acquisition of high-quality ferroelectric single crystals by selecting suitable substrates[88] or electrodes.[110] For instance, high-quality ferroelectric HZO (111) films have been successfully epitaxially stabilized on $La_{2/3}Sr_{1/3}MnO_3$ (001) electrodes.[111] Furthermore, even in cases where HZO films are polycrystalline, provided that the IP orientation is not orthogonal to the *c* axis, the IP strain can still exert an influence on the *c* axis.

4. Conclusion

In summary, we theoretically considered surface energies of various surfaces for the O- and M-phases of $Hf_{0.5}Zr_{0.5}O_2$ thin-films, which enables us to incorporate film-thickness as a dimension into the phase diagram between the two phases. Ternary phase diagrams, considering strain, electric field, and film-thickness, were thus plotted for different ways of applying strain. These results indicate that a larger portion of (111)-oriented surfaces and/or biaxial compressive strains stabilize the O-phase. A one-unit-cell thick (111) slab (~ 0.26 nm) without external strain or an $A/A_0 = 0.97$ *ac*-plane biaxial strained bulk crystal could maintain the O-phase even under strong negative electric fields of up to 0.40 V/nm. We also noticed that the (111) surface energy largely varied with respect to the oxygen chemical potential, which reminds us that the formation of oxygen vacancies, the presence of oxygen vacancies leads to a reduction in the total energy difference between the O-phase and M-phase with increasing the oxygen vacancy concentration, while the formation energy of the O-phase remains lower than that of the M-phase. Consequently, oxygen vacancy is likely to play a crucial role in tuning the relative stability of O and M phases. Such a role would help improve growth strategies for obtaining a larger portion of the O-phase in HZO thin-films. In short, we uncovered three O–M phase transition mechanisms, which allows us to provide a theoretical three-dimensional parameter-space for choosing optimal conditions to obtain the O-phase $Hf_{0.5}Zr_{0.5}O_2$ thin-films. The stabilized O-phase potentially improves performances of ultra-thin $Hf_{0.5}Zr_{0.5}O_2$ ferroelectric devices.

Data availability statement

The data that support the findings of this study are available from the corresponding author upon reasonable request.

Acknowledgements

Project supported by the Fund from the Ministry of Science and Technology (MOST) of China (Grant No. 2018YFE0202700), the National Natural Science Foundation of China (Grant Nos. 11974422 and 12104504), the Strategic Priority Research Program of the Chinese Academy of Sciences (Grant No. XDB30000000), the Fundamental Research Funds for the Central Universities, and the Research Funds of Renmin University of China (Grant No. 22XNKJ30). Calculations were performed at the Physics Lab of High-Performance Computing of Renmin University of China and the Shanghai Supercomputer Center.

References

[1] Zhang B, Meng K K, Yang M Y, Edmonds K W, Zhang H, Cai K M, Sheng Y, Zhang N, Ji Y and Zhao J H 2016 *Sci. Rep.* **6** 28458
[2] Cai K, Yang M, Ju H, Wang S, Ji Y, Li B, Edmonds K W, Sheng Y, Zhang B and Zhang N 2017 *Nat. Mater.* **16** 712
[3] Mikolajick T, Slesazeck S, Park M H and Schroeder U 2018 *MRS Bull.* **43** 340
[4] Schroeder U, Park M H, Mikolajick T and Hwang C S 2022 *Nat. Rev. Mater.* **7** 653
[5] Park M H, Lee Y H, Kim H J, Kim Y J, Moon T, Kim K D, Müller J, Kersch A, Schroeder U, Mikolajick T and Hwang C S 2015 *Adv. Mater.* **27** 1811
[6] Yu H, Chung C C, Shewmon N, Ho S, Carpenter J H, Larrabee R, Sun T, Jones J L, Ade H, O'Connor B T and So F 2017 *Adv. Funct. Mater.* **27** 1700461
[7] Si M, Saha A K, Gao S, Qiu G, Qin J, Duan Y, Jian J, Niu C, Wang H, Wu W, Gupta S K and Ye P D 2019 *Nat. Electron.* **2** 580
[8] Chen H, Zhou X, Tang L, Chen Y, Luo H, Yuan X, Bowen C R and Zhang D 2022 *Appl. Phys. Rev.* **9** 011307
[9] Shiraishi T, Katayama K, Yokouchi T, Shimizu T, Oikawa T, Sakata O, Uchida H, Imai Y, Kiguchi T, Konno T J and Funakubo H 2016 *Appl. Phys. Lett.* **108** 262904
[10] Sakashita Y, Segawa H, Tominaga K and Okada M 1993 *J. Appl. Phys.* **73** 7857
[11] Mehta R R, Silverman B D and Jacobs J T 1973 *J. Appl. Phys.* **44** 3379
[12] Li Y, Liang R, Wang J, Zhang Y, Tian H, Liu H, Li S, Mao W, Pang Y, Li Y, Yang Y and Ren T L 2017 *IEEE J. Electron. Dev. Soc.* **5** 378
[13] Cheema S S, Shanker N, Hsu S L, Rho Y, Hsu C H, Stoica V A, Zhang Z, Freeland J W, Shafer P, Grigoropoulos C P, Ciston J and Salahuddin S 2022 *Science* **376** 648
[14] Müller J, Böscke T S, Schröder U, Mueller S, Bräuhaus D, Böttger U, Frey L and Mikolajick T 2012 *Nano Lett.* **12** 4318
[15] Kim H J, Park M H, Kim Y J, Lee Y H, Jeon W, Gwon T, Moon T, Kim K D and Hwang C S 2014 *Appl. Phys. Lett.* **105** 192903
[16] Wang Y, Tao L, Guzman R, Luo Q, Zhou W, Yang Y, Wei Y, Liu Y, Jiang P, Chen Y, Lv S, Ding Y, Wei W, Gong T, Wang Y, Liu Q, Du S and Liu M 2023 *Science* **381** 558
[17] Kumar A, Mondal S and Koteswara Rao K S R 2017 *J. Appl. Phys.* **121** 085301
[18] Zhang B, Li C, Hong P and Huo Z 2021 *Appl. Phys. Lett.* **119** 022405
[19] Ruh R and Corfield P W R 1970 *J. Amer. Ceram. Soc.* **53** 126
[20] Materlik R, Künneth C and Kersch A 2015 *J. Appl. Phys.* **17** 134109
[21] Curtis C E, Doney L M and Johnson J R 1954 *J. Amer. Ceram. Soc.* **37** 458
[22] Ruh R and Patel V A 1973 *J. Amer. Ceram. Soc.* **56** 606
[23] Park M H, Lee Y H, Kim H J, Kim Y J, Moon T, Kim K D, Müller J, Kersch A, Schroeder U, Mikolajick T and Hwang C S 2015 *Adv. Mater.* **27** 1811
[24] Leger J M, Atouf A, Tomaszewski P E and Pereira A S 1993 *Phys. Rev. B* **48** 93

[25] Ohtaka O, Fukui H, Kunisada T, Fujisawa T, Funakoshi K, Utsumi W, Irifune T, Kuroda K and Kikegawa T 2001 *J. Amer. Ceram. Soc.* **84** 1369

[26] Böscke T S, Müller J, Bräuhaus D, Schröder U and Böttger U 2011 *Appl. Phys. Lett.* **99** 102903

[27] Park M H, Lee Y H, Kim H J, Kim Y J, Moon T, Kim K D, Hyun S D and Hwang C S 2018 *ACS Appl. Mater. Interfaces* **10** 42666

[28] Luo C, Yu Z, Ning H, Dong Z, Wang C, Sun L, Wu X, Wang X and Chu J 2022 *Appl. Phys. Lett.* **120** 232107

[29] Lederer M, Kämpfe T, Olivo R, Lehninger D, Mart C, Kirbach S, Ali T, Polakowski P, Roy L and Seidel K 2019 *Appl. Phys. Lett.* **115** 222902

[30] Batra R, Huan T D, Jones J L, Rossetti G and Ramprasad R 2017 *J. Phys. Chem. C* **121** 4139

[31] Lai B, Wang Y, Shao Y, Deng Y, Yang W, Jiang L and Zhang Y 2021 *J. Phys.: Condens. Matter* **33** 405402

[32] Mueller S, Mueller J, Singh A, Riedel S, Sundqvist J, Schroeder U and Mikolajick T 2012 *Adv. Funct. Mater.* **22** 2412

[33] Mueller S, Adelmann C, Singh A, Elshocht S V, Schroeder U and Mikolajick T 2012 *ECS J. Solid State Sci. Technol.* **1** N123

[34] Lomenzo P D, Takmeel Q, Zhou C, Chung C C, Moghaddam S, Jones J L and Nishida T 2015 *Appl. Phys. Lett.* **107** 242903

[35] Chen L, Zhang X, Feng G, Liu Y, Hao S, Zhu Q, Feng X, Qu K, Yang Z and Qi Y 2023 *Chin. Phys. B* **32** 108102

[36] Tromm T C U, Zhang J, Schubert J, Luysberg M, Zander W, Han Q, Meuffels P, Meertens D, Glass S, Bernardy P and Mantl S 2017 *Appl. Phys. Lett.* **111** 142904

[37] Bouaziz J, Rojo Romeo P, Baboux N, Negrea R, Pintilie L and Vilquin B 2019 *APL Mater.* **7** 081109

[38] Schroeder U, Mittmann T, Materano M, Lomenzo P D, Edgington P, Lee Y H, Alotaibi M, West A R, Mikolajick T, Kersch A and Jones J L 2022 *Adv. Electr. Mater.* **8** 2200265

[39] Torrejón L, Langenberg E, Magén C, Larrea Á, Blasco J, Santiso J, Algarabel P A and Pardo J A 2018 *Phys. Rev. Mater.* **2** 013401

[40] Schroeder U, Yurchuk E, Müller J, Martin D, Schenk T, Polakowski P, Adelmann C, Popovici M I, Kalinin S V and Mikolajick T 2014 *Jpn. J. Appl. Phys.* **53** 08LE02

[41] Müller J, Böscke T S, Müller S, Yurchuk E, Polakowski P, Paul J, Martin D, Schenk T, Khullar K, Kersch A, Weinreich W, Riedel S, Seidel K, Kumar A, Arruda T M, Kalinin S V, Schlösser T and Mikolajick T 2013 *IEEE International Electron Device Meeting* 2013 p. 10.8.1-10.8.4

[42] Cockayne E 2007 *Phys. Rev. B* **75** 094103

[43] Zhou Y, Zhang Y K, Yang Q, Jiang J, Fan P, Liao M and Zhou Y C 2019 *Comput. Mater. Sci.* **167** 143

[44] Nukala P, Ahmadi M, Wei Y, de Graaf S, Stylianidis E, Chakrabortty T, Matzen S, Zandbergen H W, Björling A, Mannix D, Carbone D, Kooi B and Noheda B 2021 *Science* **372** 630

[45] Müller J, Schröder U, Büscke T S, Müller I, Böttger U, Wilde L, Sundqvist J, Lemberger M, Kücher P, Mikolajick T and Frey L 2011 *J. Appl. Phys.* **110** 114113

[46] Hyuk Park M, Joon Kim H, Jin Kim Y, Moon T and Seong Hwang C 2014 *Appl. Phys. Lett.* **104** 072901

[47] Park M H, Kim H J, Kim Y J, Lee W, Moon T, Kim K D and Hwang C S 2014 *Appl. Phys. Lett.* **105** 072902

[48] Park M H, Kim H J, Kim Y J, Jeon W, Moon T and Hwang C S 2014 *Phys. Status Solidi (RRL) - Rapid Research Lett.* **8** 532

[49] Schroeder U, Richter C, Park M H, Schenk T, Pešić M, Hoffmann M, Fengler F P G, Pohl D, Rellinghaus B, Zhou C, Chung C C, Jones J L and Mikolajick T 2018 *Inorg. Chem.* **57** 2752

[50] Huo S, Zheng J, Liu Y, Li Y, Tao R, Lu X and Liu J 2023 *Chin. Phys. B* **32** 127701

[51] Zhou D, Xu J, Li Q, Guan Y, Cao F, Dong X, Müller J, Schenk T and Schröder U 2013 *Appl. Phys. Lett.* **103** 192904

[52] Kim H J, Park M H, Kim Y J, Lee Y H, Moon T, Kim K D, Hyun S D and Hwang C S 2016 *Nanoscale* **8** 1383

[53] Grimley E D, Schenk T, Sang X, Pešić M, Schroeder U, Mikolajick T and LeBeau J M 2016 *Adv. Electron. Mater.* **2** 1600173

[54] Pešić M, Fengler F P G, Larcher L, Padovani A, Schenk T, Grimley E D, Sang X, LeBeau J M, Slesazeck S, Schroeder U and Mikolajick T 2016 *Adv. Funct. Mater.* **26** 4601

[55] Teng C Y, Cheng C C, Li K S, Hu C, Lin J M, Lin B H, Tang M T and Tseng Y C 2023 *ACS Appl. Electron. Mater.* **5** 1114

[56] Hyuk Park M, Joon Kim H, Jin Kim Y, Lee W, Moon T and Seong Hwang C 2013 *Appl. Phys. Lett.* **102** 242905

[57] Chen W C, Tan Y F, Lin S K, Zhang Y C, Chang K C, Lin Y H, Yeh C H, Wu C W, Yeh Y H, Wang K Y, Huang H C, Tsai T M, Huang J W and Chang T C 2021 *IEEE Trans. Electron Dev.* **68** 3838

[58] Tao X, Liu L, Yang L and Xu J P 2021 *Nanotechnology* **32** 445201

[59] Wang D, Zhang Y, Guo Y, Shang Z Fu F and Lu X 2023 *Chin. Phys. B* **32** 097701

[60] Ihlefeld J F, Jaszewski S T and Fields S S 2022 *Appl. Phys. Lett.* **121** 240502

[61] Blöchl P E 1994 *Phys. Rev. B* **50** 17953

[62] Kresse G and Joubert D 1999 *Phys. Rev. B* **59** 1758

[63] Kresse G and Furthmüller J 1996 *Comput. Mater. Sci.* **6** 15

[64] Kresse G and Furthmüller J 1996 *Phys. Rev. B* **54** 11169

[65] Dion M, Rydberg H, Schröder E, Langreth D C and Lundqvist B I 2004 *Phys. Rev. Lett.* **92** 246401

[66] Klimeš J, Bowler D R and Michaelides A 2011 *Phys. Rev. B* **83** 195131

[67] Qiao J, Kong X, Hu Z X, Yang F and Ji W 2014 *Nat. Commun.* **5** 4475

[68] Hong J, Hu Z, Probert M, Li K, Lv D, Yang X, Gu L, Mao N, Feng Q, Xie L, Zhang J, Wu D, Zhang Z, Jin C, Ji W, Zhang X, Yuan J and Zhang Z 2015 *Nat. Commun.* **6** 6293

[69] Qiao J, Pan Y, Yang F, Wang C, Chai Y and Ji W 2018 *Sci. Bull.* **63** 159

[70] Hu Z X, Kong X, Qiao J, Normand B and Ji W 2016 *Nanoscale* **8** 2740

[71] Zhao Y, Qiao J, Yu P, Hu Z, Lin Z, Lau SP, Liu Z, Ji W and Chai Y 2016 *Adv. Mater.* **28** 2399

[72] Gajdoš M, Hummer K, Kresse G, Furthmüller J and Bechstedt F 2006 *Phys. Rev. B* **73** 045112

[73] Baroni S and Resta R 1986 *Phys. Rev. B* **33** 7017

[74] Tanner D S P, Janolin P E and Bousquet E 2022 *Phys. Rev. B* **106** L060102

[75] Resta R and Vanderbilt D 2007 *Physics of Ferroelectrics* (Berlin, Heidelberg: Springer) pp. 31–68

[76] Spaldin N A 2012 *J. Solid State Chem.* **195** 2

[77] King-Smith R D and Vanderbilt D 1993 *Phys. Rev. B* **47** 1651

[78] Mukhopadhyay A B, Sanz J F and Musgrave C B 2006 *Phys. Rev. B* **73** 115330

[79] Neugebauer J and Scheffler M 1992 *Phys. Rev. B* **46** 16067

[80] Zhang K, Wang C, Zhang M, Bai Z, Xie F F, Tan Y Z, Guo Y, Hu K J, Cao L, Zhang S, Tu X, Pan D, Kang L, Chen J, Wu P, Wang X, Wang J, Wang B 2020 *Nat. Nanotechnol.* **15** 1019

[81] Chen G H, Hou Z F and Gong X G 2008 *Comput. Mater. Sci.* **44** 46

[82] Yang F, Wang C, Pan Y, Zhou X, Kong X and Ji W 2019 *Chin. Phys. B* **28** 056402

[83] Duerloo K A N, Li Y and Reed E J 2014 *Nat. Commun.* **5** 4214

[84] Li B, Wan Z, Wang C, Chen P, Huang B, Cheng X, Qian Q, Li J, Zhang Z, Sun G, Zhao B, Ma H, Wu R, Wei Z, Liu Y, Liao L, Ye Y and Duan X 2021 *Nat. Mater.* **20** 818

[85] Huan T D, Sharma V, Rossetti G A and Ramprasad R 2014 *Phys. Rev. B* **90** 064111

[86] Sang X, Grimley E D, Schenk T, Schroeder U and LeBeau J M 2015 *Appl. Phys. Lett.* **106** 162905

[87] Fields S S, Cai T, Jaszewski S T, Salanova A, Mimura T, Heinrich H H, Henry M D, Kelley K P, Sheldon B W and Ihlefeld J F 2022 *Adv. Electr. Mater.* **8** 2200601

[88] Li T, Zhang N, Sun Z, Xie C, Ye M, Mazumdar S, Shu L, Wang Y, Wang D, Chen L, Ke S and Huang H 2018 *J. Mater. Chem. C* **6** 9224

[89] Estandía S, Dix N, Gazquez J, Fina I, Lyu J, Chisholm M F, Fontcuberta J and Sánchez F 2019 *ACS Appl. Electron. Mater.* **1** 1449

[90] Lee Y, Goh Y, Hwang J, Das D and Jeon S 2021 *IEEE Trans. Electron Dev.* **68** 523

[91] Cao R, Wang Y, Zhao S, Yang Y, Zhao X, Wang W, Zhang X, Lv H, Liu Q and Liu M 2018 *IEEE Electron Dev. Lett.* **39** 1207

[92] Hamouda W, Mehmood F, Mikolajick T, Schroeder U, Mentes T O, Locatelli A and Barrett N 2022 *Appl. Phys. Lett.* **120** 202902

[93] Baumgarten L, Szyjka T, Mittmann T, Materano M, Matveyev Y, Schlueter C, Mikolajick T, Schroeder U and Müller M 2021 *Appl. Phys. Lett.* **118** 032903

[94] Resta R 1994 *Rev. Mod. Phys.* **66** 899

[95] Wang X and Vanderbilt D 2007 *Phys. Rev. B* **75** 115116

[96] Souza I, Íñiguez J and Vanderbilt D 2002 *Phys. Rev. Lett.* **89** 117602

[97] Kim S J, Mohan J, Kim H S, Lee J, Young C D, Colombo L, Summerfelt S R, San T and Kim J 2018 *Appl. Phys. Lett.* **113** 182903
[98] Zhang Z, Wang C, Yang Y, Miao X and Wang X 2023 *Appl. Phys. Lett.* **122** 152902
[99] Park M H, Kim H J, Kim Y J, Lee Y H, Moon T, Kim K D, Hyun S D, Fengler F, Schroeder U and Hwang C S 2016 *ACS Appl. Mater. Interfaces* **8** 15466
[100] Chouprik A, Zakharchenko S, Spiridonov M, Zarubin S, Chernikova A, Kirtaev R, Buragohain P, Gruverman A, Zenkevich A and Negrov D 2018 *ACS Appl. Mater. Interfaces* **10** 8818
[101] Yan Y, Zhou D, Guo C, Xu J, Yang X, Liang H, Zhou F, Chu S and Liu X 2016 *J. Sol-Gel Sci. Technol.* **77** 430
[102] Yurchuk E, Müller J, Knebel S, Sundqvist J, Graham A P, Melde T, Schröder U and Mikolajick T 2013 *Thin Solid Films* **533** 88
[103] Zhao Q, Wang T, Miao Y, Ma F, Xie Y, Ma X, Gu Y, Li J, He J, Chen B, Xi S, Xu L, Zhen H, Yin Z, Li J, Ren J and Jie W 2016 *Phys. Chem. Chem. Phys.* **18** 18719
[104] Mani B K, Chang C M, Lisenkov S and Ponomareva I 2015 *Phys. Rev. Lett.* **115** 097601
[105] Liao J, Zeng B, Sun Q, Chen Q, Liao M, Qiu C, Zhang Z and Zhou Y 2019 *IEEE Electron Dev. Lett.* **40** 1868
[106] Park M H, Lee Y H, Mikolajick T, Schroeder U and Hwang C S 2018 *MRS Commun.* **8** 795
[107] Zhao D, Chen Z and Liao X 2022 *Microstructures* **2** 2022007
[108] Fengler F P G, Nigon R, Muralt P, Grimley E D, Sang X, Sessi V, Hentschel R, LeBeau J M, Mikolajick T and Schroeder U 2018 *Adv. Electr. Mater.* **4** 1700547
[109] Grimley E D, Schenk T, Mikolajick T, Schroeder U and LeBeau J M 2018 *Adv Mater. Inter.* **5** 1701258
[110] Cao J, Shi S, Zhu Y and Chen J 2021 *Physica Rapid Research Ltrs* **15** 2100025
[111] Estandía S, Dix N, Chisholm M F, Fina I and Sánchez F 2020 *Crystal Growth & Design* **20** 3801